

Article

Instrument Development: Chinese Radiometric Benchmark of Reflected Solar Band Based on Space Cryogenic Absolute Radiometer

Xin Ye ^{1,*}, Xiaolong Yi ¹, Chao Lin ¹, Wei Fang ¹, Kai Wang ¹, Zhiwei Xia ¹, Zhenhua Ji ¹, Yuquan Zheng ¹, De Sun ² and Jia Quan ³

- ¹ Changchun Institute of Optics, Fine Mechanics and Physics, Chinese Academy of Sciences, Changchun 130033, China; yxiaolong@ciomp.ac.cn (X.Y.); Linchao@ciomp.ac.cn (C.L.); fangw@ciomp.ac.cn (W.F.); wangkai@ciomp.ac.cn (K.W.); xiazw@ciomp.ac.cn (Z.X.); jizh@ciomp.ac.cn (Z.J.); zhengyq@sklao.ac.cn (Y.Z.)
- ² Changchun University of Technology, Changchun 130012, China; sunde@ccut.edu.cn
- ³ Key Laboratory of Space Energy Conversion Technologies, Technical Institute of Physics and Chemistry, Chinese Academy of Sciences, Beijing 100190, China; quanjia10@mail.ipc.ac.cn
- * Correspondence: yexin@ciomp.ac.cn; Tel.: +86-159-4305-3209

Received: 19 June 2020; Accepted: 31 August 2020; Published: 3 September 2020



Abstract: Low uncertainty and long-term stability remote data are urgently needed for researching climate and meteorology variability and trends. Meeting these requirements is difficult with in-orbit calibration accuracy due to the lack of radiometric satellite benchmark. The radiometric benchmark on the reflected solar band has been under development since 2015 to overcome the on-board traceability problem of hyperspectral remote sensing satellites. This paper introduces the development progress of the Chinese radiometric benchmark of the reflected solar band based on the Space Cryogenic Absolute Radiometer (SCAR). The goal of the SCAR is to calibrate the Earth–Moon Imaging Spectrometer (EMIS) on-satellite using the benchmark transfer chain (BTC) and to transfer the traceable radiometric scale to other remote sensors via cross-calibration. The SCAR, which is an electrical substitution absolute radiometer and works at 20 K, is used to realize highly accurate radiometry with an uncertainty level that is lower than 0.03%. The EMIS, which is used to measure the spectrum radiance on the reflected solar band, is designed to optimize the signal-to-noise ratio and polarization. The radiometric scale of the SCAR is converted and transferred to the EMIS by the BTC to improve the measurement accuracy and long-term stability. The payload of the radiometric benchmark on the reflected solar band has been under development since 2018. The investigation results provide the theoretical and experimental basis for the development of the reflected solar band benchmark payload. It is important to improve the measurement accuracy and long-term stability of space remote sensing and provide key data for climate change and earth radiation studies.

Keywords: radiometric calibration; cryogenic radiometer; reflected solar band

1. Introduction

The impact of human activities on the Earth’s ecosystem is gradually increasing. The world is facing significant environmental challenges [1,2]. The phenomena of glacier melting, sea level rise, land drought, and more extreme weather show that the climate system is changing [3,4]. Climate change is closely related to human reproduction. In the future, climate change will be more noticeable and even pose various dangers. Solar radiation, which is reflected from the Earth’s surface, clouds, etc., back to space, constitutes a powerful and highly variable feature of the climate system through changes in snow cover, sea ice, land use, aerosol, and cloud properties. Systematic and spatially resolved

observations of time series of the reflected solar spectral radiation can provide reliable analytical data for the changing climate system [5–9].

Space remote sensing technology has provided many achievements and plays a key role in meteorological prediction, disaster prevention and mitigation, resource exploration, and ocean studies [10–19]. However, climate change models need reflected solar spectral radiation data with high accuracy and long-term stability. The solar radiation changes by 0.1% within a solar cycle and changes by 0.2% within a week. The change in reflected solar spectral radiation is manifested as weakness. The measured uncertainty of reflected solar spectral radiation needs to be 1%. The measurement of reflected solar spectral radiation needs to maintain long-term stability for researching climate change trend. The decade stability needs to achieve the 0.3% level. Although the optical remote sensors are calibrated with high accuracy before being launched, the post-launch calibration cannot be traced to the International System of Units (SI), and cannot meet the absolute accuracy requirement at present [20].

Calibration is important for the development of optical remote sensors. The quality of remote sensing data can be improved by calibration [21,22]. Remote sensors can be calibrated with high accuracy before being launched. The radiometric scale can be traced back to the cryogenic absolute radiometer. However, the traceability chain of pre-launched calibration is broken by the launching process, the space environment, and model drift. The optical remote sensor must be calibrated in-orbit. The in-orbit calibration mainly adopts the solar diffuse reflector, standard lamp, and standard blackbody at present. The Moderate Resolution Imaging Spectrometer (MODIS) is one key instruments for the Earth Observing System (EOS) of National Aeronautics and Space Administration (NASA). The EOS/MODIS uses a solar diffuser to realize the highest accuracy in-orbit calibration in the field of spectral imaging. However, the measurement accuracy is only 2% [23–29]. The on-satellite radiometric scale cannot be unified due to the random attenuation of the calibration system, such as the diffuser, the standard lamp, etc. The remote sensing data of different satellites are incomparable. Thus, remote sensors cannot satisfy the urgent needs of climate change research due to the low accuracy of in-orbit radiometric calibration [30–32].

A Chinese expert group on earth observation and navigation with the 863 Project proposed the concept of a radiometric benchmark satellite in 2006 [33]. The Chinese Space-based Radiometric Benchmark (CSRB) project has been under development since 2014. The goal of the CSRB project is to launch the radiometric benchmark satellite, which adopts the new in-orbit calibration system, instead of using solar diffusers, standard lamps, vicarious calibration methods, and ground-based calibration techniques. The calibration principle of CSRB is similar to the Traceable Radiometry Underpinning Terrestrial-and Helio-Studies (TRUTHS) [34–36] as well as the Climate Absolute Radiance and Refractivity Observatory (CLARREO) [37–39]. The radiometric benchmark satellite has attained ultra-high precision tracing ability via self-calibration in orbit. The radiometric scale of the radiometric benchmark satellite is transferred to other satellites by synchronous observation of track crossing. The radiometric benchmark satellite will improve the long-term stability and the measurement accuracy of the emitted earth spectrum, the incident solar spectrum, and the reflected solar spectrum.

The development of the Chinese radiometric benchmark on the reflected solar band is introduced in this paper. The Space Cryogenic Absolute Radiometer (SCAR) was used to realize super high accuracy on-satellite radiometry while referencing the ground-based optical standard [40–46]. The reflected solar spectrum radiance is measured by the Earth–Moon Imaging Spectrometer (EMIS). The EMIS is regularly calibrated by the SCAR and the benchmark transfer chain (BTC) to improve the measurement accuracy and long-term stability. The key technologies of the space absolute radiometric measurement have been under development since 2015, such as cryogenic radiometric measurement, benchmark transfer, and hyperspectral radiance measurement.

2. The New Challenges of Spatial Radiometry

The applications of satellite remote sensing products are gradually expanding. Satellite remote sensing technology is facing greater challenges, especially in the field of climate change research.

We need to have both high accuracy and high stability data to recognize the long-term changes of the Earth. Wielicki researched the relationship between absolute calibration accuracy and the accuracy of global average decadal climate change trends [47]. The research results suggested the need for a perfect observation system as well as varying levels of instrument calibration uncertainty. The measurement uncertainty dramatically affects both climate trends and the time required to detect trends. The remote sensor should not only ensure comparability between various short-term data, but also the comparability of data across decades or even longer periods.

On-satellite calibration cannot realize traceability at present. Thus, remote sensing data are incomparable between different countries, different series of the same country, and different satellites of the same series. Total solar irradiance (TSI) is a pivotal parameter of climate models. TSI has been continuously measured on satellite platforms since 1978 [48]. The spatial TSI data from different remote sensors and different counties constitute the data chain needed to ensure long-term accuracy. Spatial TSI data have obvious 0.5% deviations between different remote sensors and different counties according to the research of Suter [49]. The World Radiation Center (WRC) established the World Radiometric Reference (WRR) to unify the solar radiometric scale in 1978. The worldwide solar absolute radiometers are traced back to the WRR by the International Pyrheliometer Comparison (IPC), which is held every five years. The TSI payloads are calibrated by the WRR transfer radiometers before being launched. Then, the uniformity of the spatial TSI data is improved from 0.5% to 0.3%. NASA developed the TSI Radiometer Facility (TRF) to calibrate the TSI radiometers using an end-to-end methodology. The TRF used the cryogenic absolute radiometer as the radiometric benchmark. TSI radiometers and cryogenic absolute radiometers measure the same incident light. The TRF provides the calibration means of TSI radiometers in vacuum-like spatial operating conditions and improves the calibration accuracy of TSI instruments [50]. The TSI measurement accuracy was further improved to 0.035%, such as the Active Cavity Radiometer Irradiance Monitor (ACRIM) launched by the ACRIM satellite (ACRIMSAT), the Total Irradiance Monitor (TIM) launched by the Solar Radiation and Climate Experiment satellite (SORCE), the Total Irradiance Monitor (TIM) launched by the U.S. Air Force Space Test Program spacecraft of the Total Solar Irradiance Calibration Transfer Experiment (TCTE), etc. [51]. However, the long-term stability of the spatial TSI data has huge uncertainty due to the lack of TSI calibration after launching. Once the data chain is broken, the absolute accuracy of spatial TSI data is negatively affected.

Spatial radiometric benchmarks must be established to improve the calibration accuracy of the remote sensing payload. The spatial applications of ultra-high accuracy measurement, such as the cryogenic absolute radiometer and phase-change blackbody, face considerable challenges. The high cost of a radiometric benchmark will exceed the cost of the payload. It is not economically feasible to equip each payload with an expensive calibration system. The benchmark satellite is an economic and effective means to solve this problem. The benchmark satellite records ultra-high accuracy measurements. The radiometric scale is transferred to other remote sensors via cross-calibration. The in-orbit calibration can ensure the comparability of multi-source remote sensing data and products. The key technologies of the space-based radiometric benchmark were researched, including the cryogenic radiometric benchmark, the phase-change blackbody, and lunar calibration. The goal of the space-based radiometric benchmark satellite is to accurately measure and calibrate the emitted earth spectrum, the incident solar spectrum, and the reflected solar spectrum.

The Chinese Radiometric Benchmark on the reflected solar band has been under development based on the SCAR. The operating models of the radiometric benchmark satellite are self-calibration, TSI calibration, uniform field calibration, and lunar calibration, as shown in Figure 1. The self-calibration model is periodically applied to check the measurement accuracy. The TSI monitor is calibrated by the synchronous measurement with the SCAR in the TSI calibration model. The remote sensors on the other satellite are calibrated by the radiometric benchmark satellite in the uniform field calibration model. When the orbits cross over uniform fields, such as deserts, lakes, and ice, the remote sensors on the other satellite are calibrated by synchronous observation under the same conditions. The moon

is also a uniform field. The cross-calibration is achieved by synchronous radiance observation of the moon.

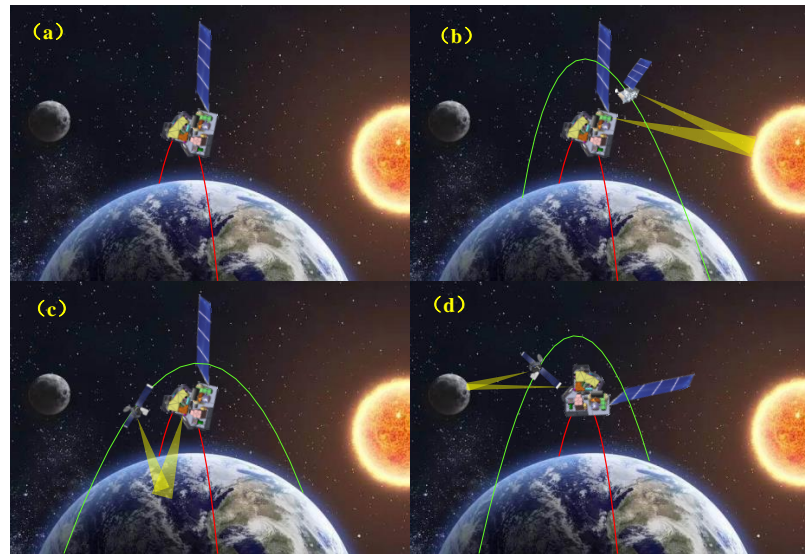


Figure 1. The working model of the radiometric benchmark satellite: (a) self-calibration, (b) total solar irradiance calibration, (c) uniform field calibration, and (d) lunar calibration.

3. Principle of Radiometric Benchmark on Reflected Solar Band

The radiometric benchmark on the reflected solar band uses the SCAR to establish the calibration system, instead of using a solar diffuser, standard lamps, vicarious calibration methods, and ground-based calibration techniques, as shown in Figure 2. The calibration system consists of the SCAR and BTC. The SCAR is an electrical substitution radiometer that works at 20 K. The detector of the SCAR is a blackbody cavity with super high absorptance. The incident light is converted into the temperature rise of the blackbody cavity by multiple reflection and absorption. The power of the incident light can be obtained by precisely measuring the electrical power when the temperature rise is replaced by electrical power. The heating effect of the incident light and electrical heater is highly equivalent at 20 K. The measurement accuracy of the SCAR is thus improved. The radiance of the Earth and moon is measured by the EMIS. The EMIS needs a high signal-to-noise ratio and a large dynamic range. The power benchmark of SCAR is converted into a radiance benchmark by the BTC. Based on the multiwavelength laser diodes and the halogen tungsten lamp, the EMIS can be calibrated by the transfer radiometer. The linearity of the EMIS can be calibrated by the sun attenuator. The goal of the radiometric benchmark on the reflected solar band is shown in Table 1. The radiance uncertainty is expected to reach 1%.

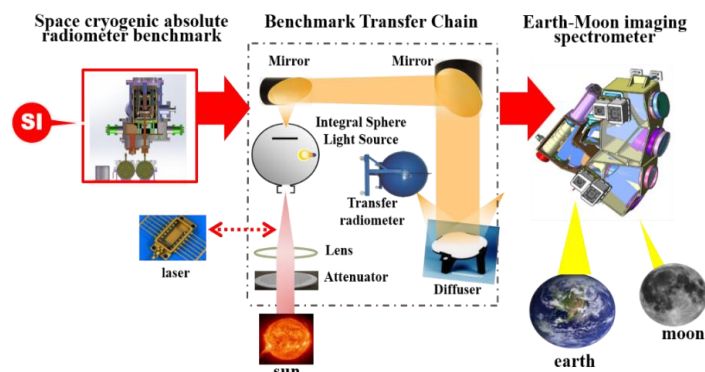


Figure 2. The principle of the radiometric benchmark on the reflected solar band.

Table 1. The goal of the radiometric benchmark on the reflected solar band. SCAR: Space Cryogenic Absolute Radiometer; EMIS: Earth–Moon Imaging Spectrometer.

Instrument	Observation Target	Parameter	Technical Indicator
SCAR	Laser	Uncertainty	0.03%
		Working temperature	20 K
		Dynamic range	1–30 mW
EMIS	Earth	Spectral range	380–2350 nm
		Radiance uncertainty	1%
		Spatial resolution	100–500 m
	Whole moon	Spectral range	380–2350 nm
		Spectral calibration uncertainty	0.5 nm
		Irradiance uncertainty	2%

3.1. SCAR

The SCAR is used to realize high accuracy radiometric measurements on satellites. The SCAR adopts the principle of the electrical substitution that has been used for nearly 100 years. The cryogenic electrical substitution measurement is the main method used for absolute radiometric calibration. The detector of the SCAR is the blackbody cavity, which has an ultra-high absorption ratio of incident light. The incident light is converted into the temperature rise of the blackbody cavity by multiple reflections and absorptions. The power of the incident light can be obtained by precisely measuring the electrical power when the temperature rise is replaced by electrical power. The incident light power (P_O) can be determined by:

$$P_O = \frac{\Delta T_O}{\Delta T_E} \cdot \frac{N V_E I_E}{\alpha \eta} \quad (1)$$

where ΔT_O is the temperature rise caused by optical power, ΔT_E is the temperature rise caused by the equivalent electrical power, α is the absorption of the blackbody cavity, N is the inequivalence coefficient, V_E is the heating voltage, I_E is the heating electric current, and η is the vacuum window transmittance. The SCAR uses cryogenic and vacuum technology to reduce the thermal noise from radiation and air convection compared with normal environmental temperature and pressure. The superconductivity application can eliminate the ohmic heat loss on the lead and improve the measurement uncertainty. The blackbody cavity is composed of oxygen-free copper. In the cryogenic condition, the thermal diffusivity of oxygen-free copper increases by four orders of magnitude, and it is possible to increase the volume for developing a blackbody cavity with an ultra-high absorption ratio. The ground-based cryogenic radiometer generally adopts a liquid helium cooled mode, and works at 4–10 K. However, the liquid helium cooled mode cannot be applied in space. The mechanical Stryn-type Pulse Tube Cryocooler (SPTC) has been under development to reduce its volume and mass and improve its working life. The SCAR was designed for a working temperature of 20 K due to the limitation of the refrigeration efficiency.

3.2. EMIS

The EMIS is used to measure the radiance of the Earth and moon. The optical design of the EMIS consists of a telescope and a hyperspectral imaging spectrometer, as shown in Figure 3. The telescope adopts a four-mirror Anastigmat (4MA) design to eliminate aberration. The 4MA consists of four aspheric mirrors. The hyperspectral imaging spectrometer adopts an Offner structure. The prism is used as the dispersion element. The telescope uses the image space telecentric structure to achieve the matching conditions with the pupil of the spectrometer. The influence of stray light is reduced by setting baffles at the intermediate image plane. The EMIS makes a trade-off between the spectral and spatial resolution, with spectral and spatial sampling that are better than 10 nm and 100 m, respectively. The swath width is about 50 km at the nadir from a 600 km orbit. The EMIS adjusts the parameters of

the lens, such as thickness and curvature. Then, the EMIS obtains a lower dispersion non-linear value and a better spectral performance is obtained.

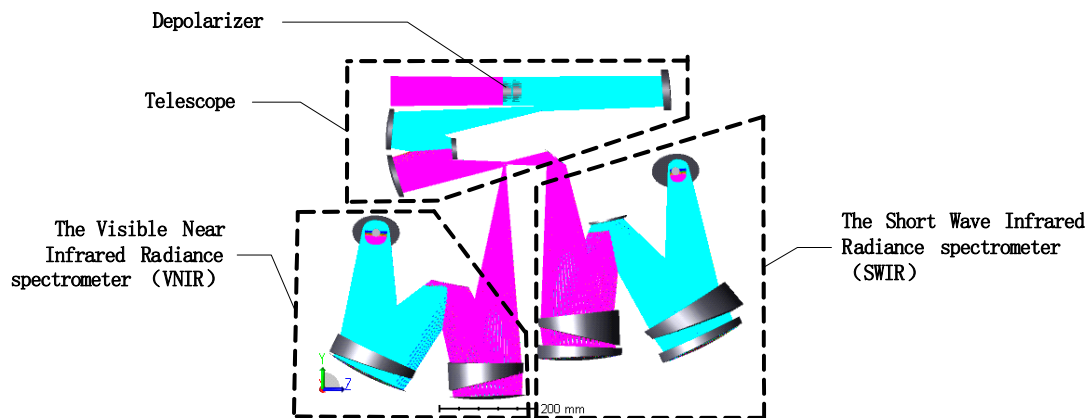


Figure 3. Optical design of the Earth–Moon Imaging Spectrometer (EMIS).

3.3. BTC

The radiometric scale of the EMIS can be traced back to the SCAR. The measurement accuracy and long-term stability of the EMIS can be improved by on-board hyperspectral calibration. The principle of hyperspectral calibration on a satellite is shown in Figure 4. The hyperspectral calibration on the satellite consists of the SCAR and the BTC. The SCAR is the primary on-board benchmark that realizes stable and highly accurate long-term radiation measurement. The transfer radiometer (TR) is calibrated and used as the working benchmark using laser power measurement and comparison. The multi-spectral radiance of the tungsten halogen lamp is calibrated by the TR. The whole spectral radiance of the tungsten halogen lamp is reconstructed using the fitting algorithm. The hyperspectral calibration of the EMIS can then be realized by the tungsten halogen lamp. The response linearity of the EMIS is calibrated by the solar attenuator.

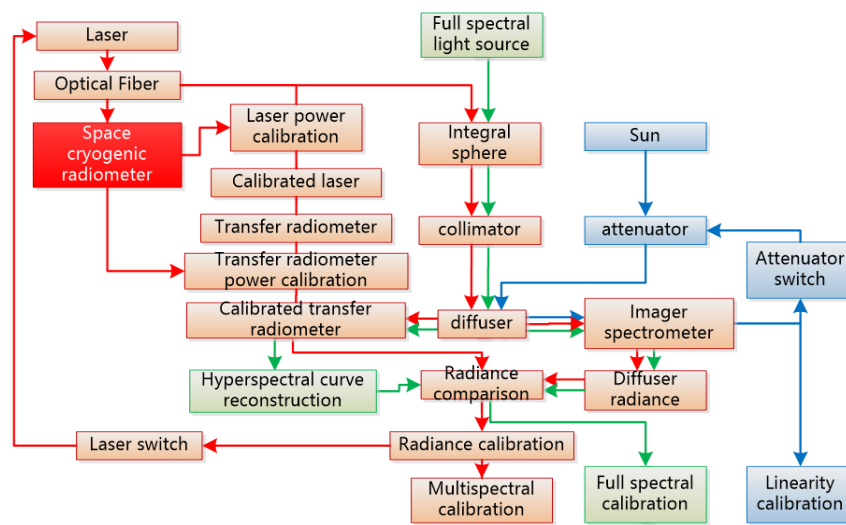


Figure 4. Principle of the benchmark transfer chain (BTC).

4. Development of Radiometric Benchmark on Reflected Solar Band

The key radiometric benchmark technologies on the reflected solar band are being researched. The prototype of the SCAR has been under development since 2015, supported by the National High-tech Research and Development Plan (the 863 Plan).

4.1. Cryogenic Absolute Measurement

The prototype of the SCAR consists of a cryogenic absolute radiation detector, the SPTC, a measurement system, and a vacuum pump, as shown in Figure 5. We have solved the problems of radiation heat leakage, high thermal resistance connection, and cryogenic refrigeration. The sensitivity of the blackbody cavity achieved 3.95 K/mW. The blackbody cavity was designed according to Fang's effective emissivity simulation results. The blackbody cavity adopts the cylindrical cavity with a cone bottom to increase the reflection times of the incident light. The internal surface of the blackbody cavity is sprayed with black paint. Experimental measurement results illustrated that the blackbody cavity absorption is 0.999928 ± 0.000006 (1σ) at a wavelength of 632 nm [52–55].

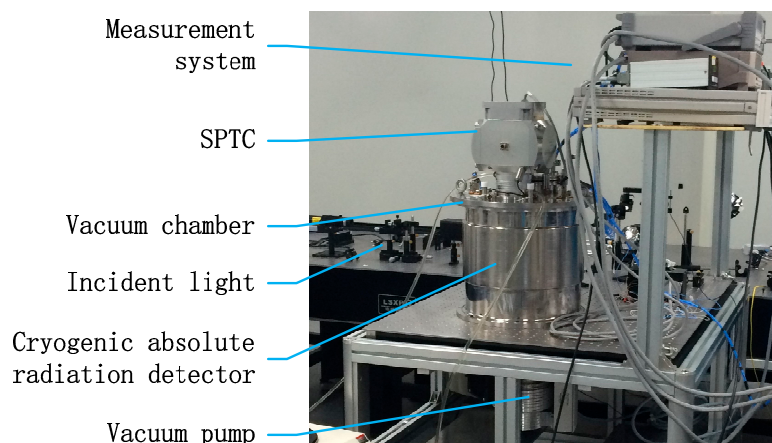


Figure 5. The Space Cryogenic Absolute Radiometer (SCAR) prototype. SPTC: Stryn-type Pulse Tube Cryocooler.

The 20 K cryogenic working temperature is obtained by the SPTC. The SPTC has three advantages, (a) small volume, (b) little vibration, and (c) a long working life. The core component of SPTC is the compressor. The working gas is compressed into liquid and absorbs the heat of the pulse tube. The heat quantity of the cool head is exported by the pulse tube. The SPTC uses a coaxial configuration to facilitate the coupling between the cool head and the absolute radiation receiver. The pulse tube and the compressor are combined together to reduce the volume. The experimental results illustrated that the cryogenic platform temperature stabilizes at 21.8 K and the temperature stability of the cryogenic platform is 13 mK. The temperature stability of the SPTC is the main thermal noise for the blackbody cavity. The spaceborne SPTC is being developed to provide a refrigerating capacity of 350 mW at 20 K.

The three-stage heat transfer structure is designed for the connection between the blackbody cavity and the SPTC. The three-stage heat transfer structure consists of a main heat sink, a temperature-controlled heat sink, and a cryogenic platform. The two-stage precise temperature controller is designed based on the Proportional Integral Differential (PID) algorithm to establish a high stable thermal environment for the blackbody cavity. The temperature stability of the main heat sink was improved from 13 to 0.5 mK. The high stability of the working environment in the 20 K temperature region was thus established. The thermoelectric repeatability of the blackbody cavity was experimentally tested. The blackbody cavity was repeatedly heated by a group of electrical powers. The electrical power was increased gradually from 0.1 to 1 mW. The increase in electrical power was 0.1 mW. The temperature response curves were measured and the equilibrium temperatures were obtained as shown in Figure 6. The experimental results illustrated that the thermoelectric repeatability of the blackbody cavity is 0.1 mK with different electrical power inputs. The thermoelectric repeatability is optimized by the improvement in environmental stability.

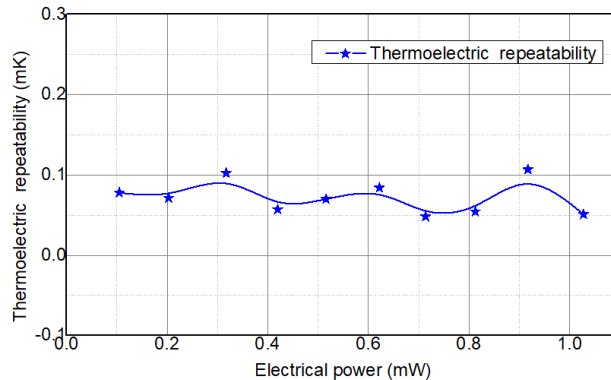


Figure 6. Thermoelectric repeatability of blackbody cavity.

The SCAR adopts the measurement algorithm of double electrical calibration. The non-linearity of sensitivity is compensated by a linear fitting in a small power region. The measurement repeatability of the SCAR is 0.019% for 0.4 mW of incident light. The synthetic uncertainty of the SCAR is 0.021% according to the experimental measurements and theoretical analysis. The standard uncertainty of the SCAR is 0.029% by combining the repeatability uncertainty and synthetic uncertainty. The standard uncertainty of the SCAR was tested by the indirect comparison with the cryogenic radiometer of the National Institute of Metrology (NIM).

Therefore, the high accuracy optical power measurement can be realized via SCAR. The payload prototype of SCAR is being developed to establish the radiometric satellite benchmark.

4.2. Whole Spectral Light Source

Whole spectral light is needed for the full spectral radiance calibration of the EMIS. We adopted a tungsten halogen lamp with a smooth spectral distribution curve as the whole spectral light source. The spectral distribution curve of the tungsten halogen lamp can be precisely obtained using an inversion algorithm according to the multispectral calibration data. The spectral radiance measurement system was established. The long time-scale variation of the spectral distribution curve has been experimentally measured. The spectral radiance attenuation of the tungsten halogen lamp was obtained as shown in Figure 7. The experimental results illustrated that the spectral radiance achieves red shift with time. The results provide key support for inversion algorithm investigation.

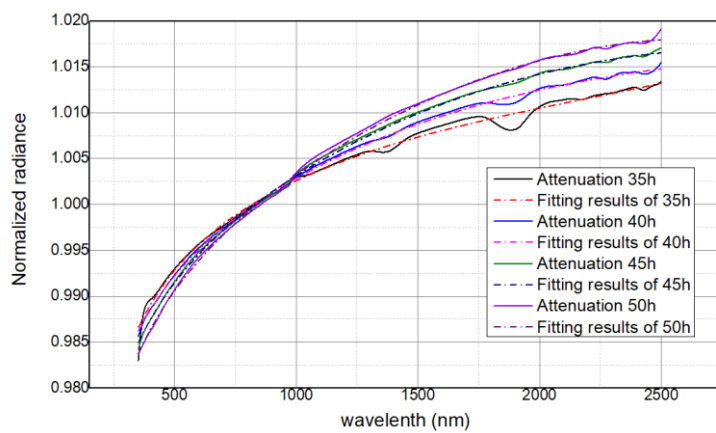


Figure 7. Spectral radiance attenuation of a tungsten halogen lamp.

The tungsten halogen lamp is similar to the high temperature blackbody. Huang established an inversion algorithm which considers the impact of emissivity [56]. When the fitting parameters (c_0, c_1 ,

c_2, c_3, c_4, c_5) are determined via multispectral calibration, the spectral radiance of the full spectral band ($F(\lambda)$) was obtained, which is expressed as:

$$F(\lambda) = \begin{cases} \lambda^{-5} \exp(c_0 + c_1/\lambda) \times \exp[c_2\lambda - c_3|\frac{\lambda-450}{500}|^{c_4}] (\lambda < 450) \\ \lambda^{-5} \exp(c_0 + c_1/\lambda) \times \exp[c_2\lambda + c_5|\frac{\lambda-450}{500}|^{c_6}] (\lambda > 450) \end{cases} \quad (2)$$

According to Formula (2), the spectral radiance of the standard lamp was rebuilt as shown in Figure 8. The average relative error of the rebuilt spectral radiance was 0.6%. We are researching the inversion algorithm to reduce the average relative error from 0.6% to 0.3%.

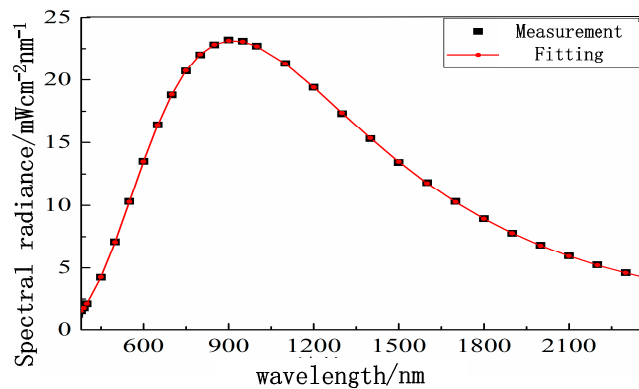


Figure 8. Spectral radiance inversion of the tungsten halogen lamp.

The long-term spectral radiance data of tungsten halogen lamp are accumulated for researching the attenuation property. The tungsten halogen lamp can be used as the whole spectral light source for the radiometric benchmark on the reflected solar band. The inversion algorithm of the full spectral band radiance has been investigated, and needs optimization to reduce the error.

4.3. Signal-to-Noise Ratio (SNR) Analysis of EMIS

The SNR equation of the Visible Near Infrared Radiance spectrometer (VNIR) is depicted by:

$$SNR_{VNIR} = \frac{S_{eVNIR}(\lambda)}{\sqrt{S_{eVNIR}(\lambda) + N_e^2 + N_{OP}^2 + N_{AD}^2}} \quad (3)$$

where N_e is the electrical noise, N_{OP} is the amplifier noise, N_{AD} is the analog-to-digital converter noise and $S_{eVNIR}(\lambda)$ is the signal electric number of VNIR, which is expressed by:

$$S_{eVNIR}(\lambda) = \frac{\pi A_d}{4F^2} \cdot \frac{\lambda}{hC} \cdot T_{in} \cdot \tau_0(\lambda) \cdot L_{VNIR}(\lambda) \cdot \eta(\lambda) \cdot \Delta\lambda \quad (4)$$

where F is the focal length, $\tau_0(\lambda)$ is the transmittance of the front optical system, $\eta(\lambda)$ is the transmittance of the VNIR, $\Delta\lambda$ is the spectral resolution, and $L_{VNIR}(\lambda)$ is the pupil radiance of the VNIR optical system. Under typical conditions, the pupil radiance is as shown in Figure 9a. According to Formula (4), the signal electric number of VNIR is as shown in Figure 9c. The SNR of the VNIR spectrometer is better than 300, as shown in Figure 9e.

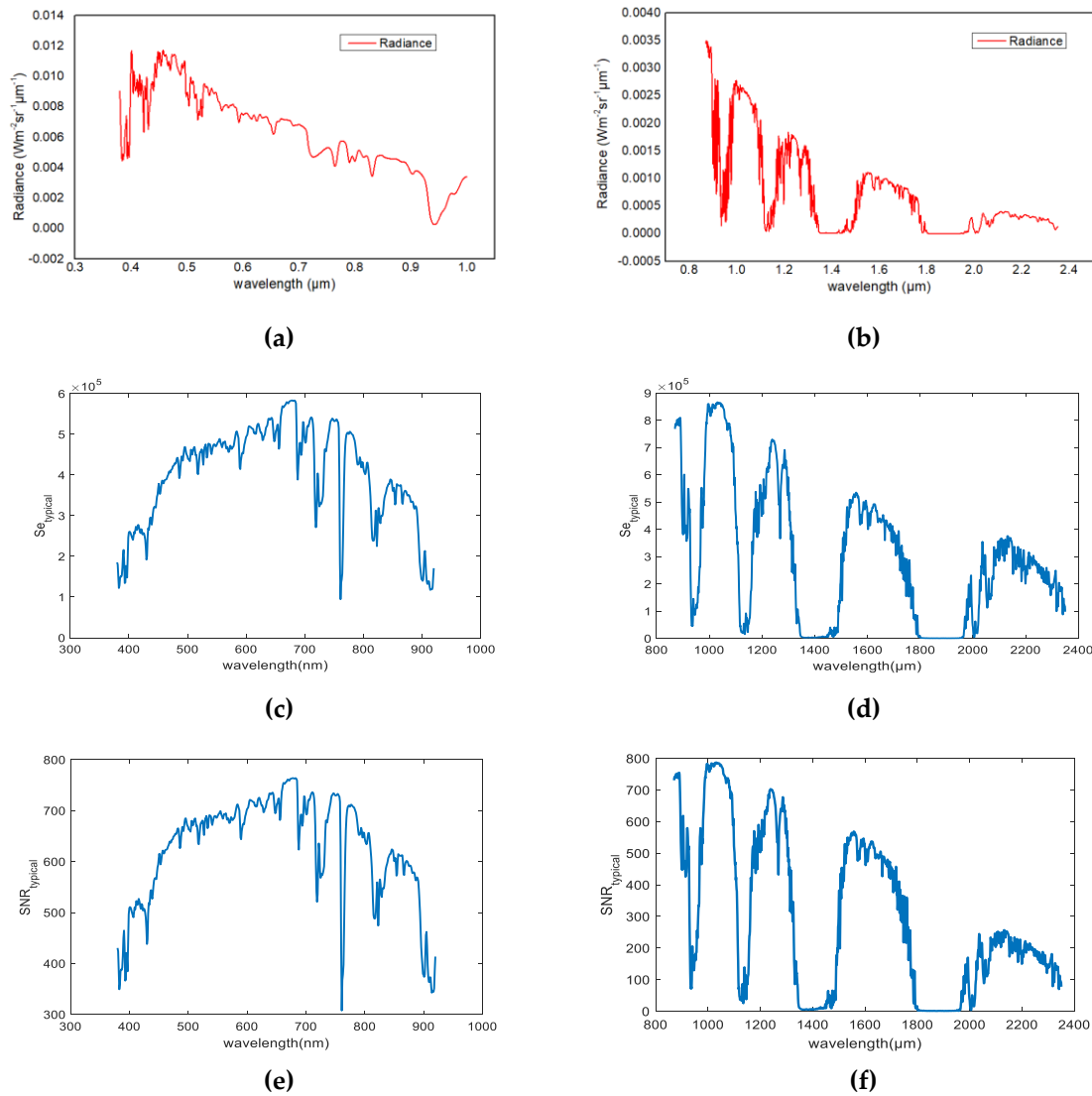


Figure 9. Signal-to-noise ratio (SNR) simulation results: (a) pupil radiance of Visible Near Infrared Radiance spectrometer (VNIR), (b) pupil radiance of the Short Wave Infrared Radiance spectrometer (SWIR), (c) signal electric number of VNIR, (d) signal electric number of SWIR, (e) VNIR spectrometer SNR, and (f) SWIR spectrometer SNR.

Considering the thermal radiation noise of the instrument (S_T), the SNR equation of the Short Wave Infrared Radiance spectrometer (SWIR) is depicted by:

$$SNR_{SWIR} = \frac{S_{eSWIR}(\lambda)}{\sqrt{S_{eSWIR}(\lambda) + S_T + N_e^2 + N_{OP}^2 + N_{AD}^2}} \quad (5)$$

where S_T is the environment thermal noise, and $S_{eSWIR}(\lambda)$ is the signal electric number of SWIR, which is depicted by:

$$S_{eSWIR}(\lambda) = \frac{\pi A_d}{4F^2} \cdot \frac{\lambda}{hC} \cdot T_{in} \cdot \tau_0(\lambda) \cdot L_{SWIR}(\lambda) \cdot \eta(\lambda) \cdot \Delta\lambda \quad (6)$$

where F is the focal length, $\tau_0(\lambda)$ is the transmittance of the front optical system, $\eta(\lambda)$ is the transmittance of the SWIR, $\Delta\lambda$ is the spectral resolution and $L_{SWIR}(\lambda)$ is the pupil radiance of the SWIR optical system. The pupil radiance is shown in Figure 9b at the typical condition. The signal electric number is shown

in Figure 9d. The SNR of the SWIR spectrometer is better than 300 at the non-absorption region, as shown in Figure 9e.

The measurement repeatability (σ) of EMIS can be calculated as:

$$\sigma = \frac{1}{SNR} \quad (7)$$

The SNR analysis results of the VNIR and SWIR spectrometers illustrated that the radiance measurement repeatability of EMIS is better than 0.3%. The optical design can meet the requirements of high-precision hyperspectral remote sensing.

4.4. Polarization Correction

The dual Babinet depolarizer is used by the telescope to reduce the polarization sensitivity of the optical system. The dual Babinet depolarizer consists of a two-series Horizontal-Vertical (H-V) depolarization device. The Muller matrix of the first H-V depolarization device is expressed as:

$$M = \begin{bmatrix} 1 & 0 & 0 & 0 \\ 0 & 1 & 0 & 0 \\ 0 & 0 & \cos \delta_1 x & \sin \delta_1 x \\ 0 & 0 & -\sin \delta_1 x & \cos \delta_1 x \end{bmatrix} \quad (8)$$

and $\delta_1 x$ is depicted by:

$$\begin{aligned} \delta_1 x &= \frac{2\pi}{\lambda} [n_0(\lambda) - n_e(\lambda)] [(t_1 - rx \tan \beta) - (t_2 + rx \tan \beta)] \\ &= k \Delta n(\lambda) [2rx \tan \beta + (t_1 - t_2)] \end{aligned} \quad (9)$$

where λ is the wavelength, x is the normalized position coordinates, n_o is the refractive index of O light, n_e is the refractive index of X light, r is the radius of depolarizer, and β is the angle between the two wedge plates.

The second H-V depolarization device is placed behind the first H-V depolarization device. The angle between the two depolarizers is 45°. The Muller matrix of the second H-V depolarization device is expressed as:

$$M_{45} = R_{45} M_0 R_{-45} = \begin{bmatrix} 1 & 0 & 0 & 0 \\ 0 & \cos \delta_2 x' & 0 & \sin \delta_2 x' \\ 0 & 0 & 1 & 0 \\ 0 & -\sin \delta_2 x' & 0 & \cos \delta_2 x' \end{bmatrix} \quad (10)$$

The Muller matrix of the dual Babinet depolarizer is:

$$D = MM_{45} = \begin{bmatrix} 1 & 0 & 0 & 0 \\ 0 & \cos \delta_2 x' & -\sin \delta_2 x' \sin \delta_1 x & \cos \delta_1 x \sin \delta_2 x' \\ 0 & 0 & \cos \delta_1 x & \sin \delta_1 x \\ 0 & -\sin \delta_2 x' & -\cos \delta_2 x' \sin \delta_1 x & \cos \delta_2 x' \cos \delta_1 x \end{bmatrix} \quad (11)$$

Each beam incident on the depolarizer is described by Formula (5). After polar integration, the spatial average Muller matrix of a circular incident beam is expressed as:

$$M_{\text{Entering pupil}} = \begin{bmatrix} 1 & 0 & 0 & 0 \\ 0 & A & B & D \\ 0 & 0 & A & 0 \\ 0 & 0 & D & C \end{bmatrix} \quad (12)$$

$$A = \frac{1}{\pi} \int_0^1 \rho d\rho \int_0^{2\pi} \cos[\delta_2 \rho \cos(\theta + \frac{\pi}{4})] d\theta \quad (13)$$

$$B = \frac{1}{\pi} \int_0^1 \rho d\rho \int_0^{2\pi} \sin(\delta_1 \rho \cos \theta) \sin[\delta_2 \rho \cos(\theta + \frac{\pi}{4})] d\theta \quad (14)$$

$$C = \frac{1}{\pi} \int_0^1 \rho d\rho \int_0^{2\pi} \cos(\delta_1 \rho \cos \theta) \cos[\delta_2 \rho \cos(\theta + \frac{\pi}{4})] d\theta \quad (15)$$

$$D = 0 \quad (16)$$

Considering that the parameters of the two H-V depolarization devices are coincident, $\delta = \delta_1 = \delta_2$, Formulas (7)–(10) can be simplified as:

$$A = 2 \frac{J_1(\delta)}{\delta} \quad (17)$$

$$B = \frac{J_1(2\delta \sin \frac{\pi}{8})}{2\delta \sin \frac{\pi}{8}} - \frac{J_1(2\delta \cos \frac{\pi}{8})}{2\delta \cos \frac{\pi}{8}} \quad (18)$$

$$C = \frac{J_1(2\delta \sin \frac{\pi}{8})}{2\delta \sin \frac{\pi}{8}} + \frac{J_1(2\delta \cos \frac{\pi}{8})}{2\delta \cos \frac{\pi}{8}} \quad (19)$$

The Stokes vector of an arbitrary polarized light is:

$$E = \begin{bmatrix} 1 \\ \cos 2\theta \\ \sin 2\theta \\ 0 \end{bmatrix} \quad (20)$$

Then, the Stokes vector of the outgoing light is:

$$F' = \begin{bmatrix} 1 & 0 & 0 & 0 \\ 0 & A & B & D \\ 0 & 0 & A & 0 \\ 0 & 0 & D & C \end{bmatrix} \cdot \begin{bmatrix} 1 \\ \cos 2\theta \\ \sin 2\theta \\ 0 \end{bmatrix} = \begin{bmatrix} 1 \\ A \cdot \cos 2\theta + B \cdot \sin 2\theta \\ A \cdot \sin 2\theta \\ 0 \end{bmatrix} \quad (21)$$

According to the calculation formula of the degree of polarization of light wave, which is expressed as:

$$P = \sqrt{(Q^2 + U^2 + V^2)/I^2} \quad (22)$$

the residual degree of polarization of the dual Babinet depolarizer is:

$$P = \sqrt{(A \cdot \cos 2\theta + B \cdot \sin 2\theta)^2 + (A \cdot \sin 2\theta)^2} \quad (23)$$

Based on the theoretical model, the residual polarization degree of the depolarizer is designed to 2% ($\lambda = 920$ nm).

5. Discussion

The uncertainty of the radiometric benchmark on the reflected solar band is analyzed in this section. The uncertainty decomposition is shown in Table 2. The radiometric uncertainty of the SCAR is 0.03%. The radiance uncertainty of the EMIS is 0.3%. Thus, the uncertainty of the radiance calibration is expected to reach 0.5% to realize hyperspectral radiance measurement with less than 1% uncertainty.

Table 2. Reflected solar spectrum observation uncertainty.

Components	Impact Factor	Value
SCAR	Radiometric uncertainty	0.03%
Radiance Calibration		0.5%
Laser diode	Power stability	0.1%
Transfer radiometer	Optical power measurement	0.1%
	Optical-radiance conversion	0.08%
	Radiance measurement	0.1%
	Photodiode detector	0.14%
Full spectral light	Spectral radiance stability	0.2%
	Spectral radiance reconstruction	0.3%
Diffuser	Reflection uniformity	0.15%
	Stray light	0.2%
EMIS	Radiance uncertainty	0.3%
Total		0.6%

The laser diodes with 10 wavelengths are coupled by optical fibers. The radiometric scale of the CSAR is transferred to the TR by measuring the multiwavelength laser diodes separately. The impact factors conclude the power stability of the laser diodes (u_1) and the optical power measurement uncertainty of the TR (u_2). Then, the TR is used as the secondary standard in radiance calibration. The radiometric scale is converted from power to radiance by the TR. The spectral curve of the tungsten halogen lamp is corrected by multispectral calibration and a spectral reconstruction algorithm. The light of the tungsten halogen lamp is reflected by the diffuser, and measured by the TR and the EMIS with the same angle. Then, the EMIS can be calibrated by the TR. The uncertainty impact factors conclude the uncertainty of the optical-radiance conversion (u_3), radiance measurement (u_4), photodiode detector (u_5), spectral radiance stability (u_6), spectral radiance reconstruction accuracy (u_7), diffuser reflection uniformity (u_8), and stray light (u_9).

6. Conclusions

The radiometric benchmark on the reflected solar band has been under development to improve the accuracy and long-term stability of the hyperspectral radiance data for climate change research. The radiometric benchmark was designed based on the SCAR referencing the ground-based optical standard. The radiometric scale of the SCAR is converted and transferred by the TR. The TR is used as the secondary standard in radiance calibration. The EMIS is calibrated in-orbit to improve the measurement accuracy and long-term stability.

The SCAR is used to record highly accurate light power measurements on satellites. The SCAR is an electrical substitution radiometer, and it works at 20 K. The prototype of the SCAR consists of an absolute radiation receiver, the SPTC, a measurement system, and a vacuum pump. The experimental results illustrated that the measurement uncertainty is 0.029% for 0.4 mW incident light. The uncertainty was tested by an indirect comparison with the cryogenic radiometer of the NIM.

The EMIS measures the hyperspectral radiance of the Earth and the moon. The optical design of the EMIS consists of a telescope and a hyperspectral imaging spectrometer. The telescope adopts the four-mirror anastigmat (4MA) design to eliminate aberration. The 4MA consists of four aspheric mirrors. The dual Babinet depolarizer is used by the telescope to reduce the polarization sensitivity of the optical system. The hyperspectral imaging spectrometer adopts an Offner structure. The prism is used as the dispersion element. The SNR of the SWIR and VNIR spectrometers is improved to 300 by optimizing the optical design.

The BTC is used to realize the calibration of multispectral, whole spectral, and linearity calibration. The BTC consists of the TR, multiwavelength laser diodes, a tungsten halogen lamp, a diffuser, and a

solar attenuator. The TR is used to convert the benchmark from the light power to radiance. The EMIS is calibrated by the tungsten halogen lamp and TR based on the hyperspectral curve reconstruction. The EMIS is calibrated in-orbit by the BTC to improve the measurement accuracy and long-term stability.

The uncertainty decomposition of the radiometric benchmark on the reflected solar band was analyzed. The radiometric uncertainty of the SCAR is 0.03%. The radiance uncertainty of the EMIS is 0.3%. Thus, the uncertainty of the radiance calibration is expected to reach 0.5% to realize less than 1% uncertainty of hyperspectral radiance measurements.

The results provide the theoretical and experimental basis for the payload design of the radiometric benchmark on the reflected solar band. The radiometric benchmark will significantly improve the measurement accuracy and long-term stability of hyperspectral radiance, and provide remote sensing data for climate change research. The radiometric scale can be transferred to the remote sensors on the other satellites via track crossing calibration over uniform fields.

Author Contributions: Formal analysis, C.L., K.W., Z.X., Z.J., Y.Z. and J.Q.; Project administration, X.Y. (Xin Ye) and W.F.; Software, D.S.; Writing—original draft, X.Y. (Xiaolong Yi); Writing—review & editing, X.Y. (Xin Ye). All authors have read and agreed to the published version of the manuscript.

Funding: This research was funded by the National Key R&D Program of China under grant 2018YFB0504600, 2018YFB0504603.

Acknowledgments: The authors thank numerous staff members at the Changchun Institute of Optics, Fine Mechanics and Physics, the Chinese Academy of Sciences, including Song Baoqi, Jia Ruidong, Zheng Siqiao, Wu Duo, and many others. The authors thank Yu Bingxi, former project leader of Solar Irradiance Absolute Radiometer (SIAR), for his great contributions and guidance. The authors also thank the referees for generous help and good comments.

Conflicts of Interest: The authors declare no conflict of interest. The overall project plan design was made by Xin Ye. Xiaolong Yi is in charge of the development of the space cryogenic absolute radiometer. Chao Lin is in charge of the development of the Earth–Moon Imaging Spectrometer. Wei Fang designs the benchmark transfer chain. Kai Wang designs the mechanical structure of the space cryogenic absolute radiometer. Zhiwei Xia designs the optical structure of the space cryogenic absolute radiometer. Zhenhua Ji designs the optical structure of the Earth–Moon Imaging Spectrometer. Yuquan Zhen provides the signal to noise ratio analysis data. De Sun develops the blackbody cavity. Jia Quan designs the mechanical stryn-type pulse tube cryocooler.

References

1. Bouchereau, A.; Aziz, A.; Larher, F.; Tanguy, M.J. Polyamines and environmental challenges: Recent development. *Plant Sci.* **1999**, *140*, 103–125. [[CrossRef](#)]
2. Brauch, H.G. Introduction: Globalization and Environmental Challenges: Reconceptualizing Security in the 21st Century. *Glob. Environ. Chall.* **2008**, *3*, 27–43.
3. Niklas, S. The Indonesian Throughflow and the Global Climate System. *J. Clim.* **1998**, *11*, 676–689.
4. Melillo, J.M. Soil Warming and Carbon-Cycle Feedbacks to the Climate System. *Science* **2002**, *298*, 2173–2176. [[CrossRef](#)] [[PubMed](#)]
5. Loeb, N.G.; Wielicki, B.A.; Doelling, D.R.; Smith, G.L.; Keyes, D.F.; Kato, S.; Smith, N.M.; Wong, T. Optimal Closure of the Earth’s Top-of-Atmosphere Radiation Budget. *J. Clim.* **2009**, *22*, 748–766. [[CrossRef](#)]
6. Schlifkowitz, U.; Finsterle, W.; Schmutz, W. Development of a phase-sensitive absolute radiometer for space and ground-based use. In *17th ESA Symposium on European Rocket and Balloon Programmes and Related Research*; ESA: Paris, France, 2005; Volume 590, pp. 467–469.
7. Baum, B.A.; Wielicki, B.A. Cirrus Cloud Retrieval Using Infrared Sounding Data: Multilevel Cloud Errors. *J. Appl. Meteorol.* **1994**, *33*, 107–117. [[CrossRef](#)]
8. Hu, X.Q.; Xu, N.; Weng, F.Z.; Zhang, Y.; Student Member IEEE; Chen, L.; Zhang, P. Long-Term Monitoring and Correction of FY-2 Infrared Channel Calibration Using AIRS and IASI. *IEEE Trans. Geosci. Remote Sens.* **2013**, *51*, 5008–5018. [[CrossRef](#)]
9. McClain, C.R.; Signorini, S.R.; Christian, J.R. Subtropical gyre variability observed by ocean-color satellites. *Deep Sea Res. Part II Top. Stud. Oceanogr.* **2004**, *51*, 281–301. [[CrossRef](#)]

10. Cook, B.I.; Pau, S. A Global Assessment of Long-Term Greening and Browning Trends in Pasture Lands Using the GIMMS LAI3g Dataset. *Remote Sens.* **2013**, *5*, 2492–2512. [[CrossRef](#)]
11. Tazio, S.; Christian, A.; Hugo, R. Interpretation of Aerial Photographs and Satellite SAR Interferometry for the Inventory of Landslides. *Remote Sens.* **2013**, *5*, 2554–2570.
12. Jing, Y.Y.; Zhang, Y.C.; Hu, M.Q.; Chu, Q.; Ma, R.H. MODIS-Satellite-Based Analysis of Long-Term Temporal-Spatial Dynamics and Drivers of Algal Blooms in a Plateau Lake Dianchi, China. *Remote Sens.* **2019**, *11*, 2582. [[CrossRef](#)]
13. Lee, Z.P.; Miroslaw, D.; Kendeall, L.C.; Curtiss, O.D.; Dariusz, S.W.; Joseph, R. Diffuse attenuation coefficient of downwelling irradiance: An evaluation of remote sensing methods. *J. Geophys. Res. Ocean.* **2005**, *110*, C2. [[CrossRef](#)]
14. Bardia, Y.; Saeed, S.; Clemente, I.C.; Xavier, P.V.M.; Georges, B.; Martin, C. Continuum removal for ground-based LWIR hyperspectral infrared imagery applying non-negative matrix factorization. *Appl. Opt.* **2018**, *57*, 6219–6228.
15. Lee, Z.P.; Du, K.P.; Robert, A. A model for the diffuse attenuation coefficient of downwelling irradiance. *J. Geophys. Res. Ocean.* **2005**, *110*, C02016. [[CrossRef](#)]
16. Yousefi, B.; Sojasi, S.; Castanedo, C.I.; Beaudoin, G.; Huot, F.; Maldaque, X.P.V.; Chamberland, M.; Lalonde, E. Emissivity retrieval from indoor hyperspectral imaging of mineral grains. In Proceedings of the SPIE Commercial Scientific + Sensing and Imaging, Baltimore, MD, USA, 11 May 2016.
17. Simon, A.; Shanmugam, P. Estimation of the spectral diffuse attenuation coefficient of downwelling irradiance in inland and coastal waters from hyperspectral remote sensing data: Validation with experimental data. *Int. J. Appl. Earth Obs. Geoinf.* **2016**, *49*, 117–125. [[CrossRef](#)]
18. Gordon, H.R.; Mccluney, W.R. Estimation of the Depth of Sunlight Penetration in the Sea for Remote Sensing. *Appl. Opt.* **1975**, *14*, 413–416. [[CrossRef](#)]
19. Ruddick, K.G.; Voss, K.; Banks, A.C.; Boss, E.; Castagna, A.; Frouin, R.; Hieronymi, M.; Jamet, C.; Johnson, B.C.; Kuusk, J.; et al. A Review of Protocols for Fiducial Reference Measurements of Downwelling Irradiance for the Validation of Satellite Remote Sensing Data over Water. *Remote Sens.* **2019**, *11*, 1742. [[CrossRef](#)]
20. Hu, X.Q.; Zhang, Y.X.; Liu, Z.Q.; Zhang, G.S.; Huang, Y.B.; Qiu, K.M.; Wang, Y.K.; Zhang, L.J.; Zhu, X.B.; Rong, Z.G. Optical characteristics of China Radiometric Calibration Site for Remote Sensing Satellite Sensors (CRCRSSS). In *Hyperspectral Remote Sensing of the Land and Atmosphere*; International Society for Optics and Photonics: Washington, DC, USA, 2001.
21. Xiong, J.; Cao, C.; Chander, G. An overview of sensor calibration inter-comparison and applications. *Front. Earth Sci. China* **2010**, *4*, 237–252. [[CrossRef](#)]
22. Cooksey, C.; Datla, R. Workshop on Bridging Satellite Climate Data Gaps. *J. Res. Natl. Inst. Stand. Technol.* **2011**, *116*, 505–516. [[CrossRef](#)]
23. Xiong, X.; Barnes, W.; Chiang, K.; Erives, H.; Che, N.; Sun, J.; Isaacman, A.; Salomonson, V. Status of Aqua MODIS on-orbit calibration and characterization. *Proc. SPIE* **2004**, *5570*, 317–327.
24. Xiong, X.; Sun, J.Q.; Esposito, J.A.; Guenther, B.; Barnes, W. MODIS reflective solar bands calibration algorithm and on-orbit performance. *Proc. SPIE* **2003**, *4891*, 95–104.
25. Guenther, B.; Barnes, W.; Knight, E.; Barker, J.; Harnden, J.; Weber, R.; Roberto, M.; Godden, G.; Montgomery, H.; Abel, P. MODIS Calibration: A Brief Review of the Strategy for the At-Launch Calibration Approach. *J. Atmos. Ocean. Technol.* **1996**, *13*, 274–285. [[CrossRef](#)]
26. Xu, N.; Chen, L.; Hu, X.Q.; Zhang, L.Y.; Zhang, P. Assessment and Correction of on-Orbit Radiometric Calibration for FY-3 VIRR Thermal Infrared Channels. *Remote Sens.* **2014**, *6*, 2884–2897. [[CrossRef](#)]
27. Xiong, X.; Butler, J.; Chiang, K.; Efremova, B.; Fulbright, J.; Lei, N.; McIntire, J.; Wang, Z. VIIRS On-Orbit Calibration and Performance Update IGARSS 2014–2014 IEEE International Geoscience and Remote Sensing Symposium; IEEE: Piscataway Township, NJ, USA, 2014.
28. Sun, J.; Xiong, X.; Butler, J. *NPP VIIRS On-Orbit Calibration and Characterization Using the Moon Earth Observing Systems XVII*; International Society for Optics and Photonics: Washington, DC, USA, 2012.
29. Kouyama, T.; Kato, S.; Kikuchi, M.; Sakuma, F.; Miura, A.; Tachikawa, T.; Tsuchida, S.; Obata, K.; Nakamura, R. Lunar Calibration for ASTER VNIR and TIR with Observations of the Moon in 2003 and 2017. *Remote Sens.* **2019**, *11*, 2712. [[CrossRef](#)]

30. Loeb, N.G.; Wielicki, B.A.; Wong, T.; Parker, P.A. Impact of data gaps on satellite broadband radiation records. *J. Geophys. Res. Atmos.* **2009**, *114*, D11. [[CrossRef](#)]
31. Poncet, A.M.; Knappenberger, T.; Brodbeck, C.; Michael, F.J.; Shaw, J.N.; Ortiz, B.V. Multispectral UAS Data Accuracy for Different Radiometric Calibration Methods. *Remote Sens.* **2019**, *11*, 1917. [[CrossRef](#)]
32. Gallo, K.; Stensaas, G.; Dwyer, J.; Longhenry, R. A Land Product Characterization System for Comparative Analysis of Satellite Data and Products. *Remote Sens.* **2018**, *10*, 48. [[CrossRef](#)]
33. Wang, Y.P.; Hu, X.Q.; Wang, H.R.; Ye, X.; Fang, W. Standard transfer chain for radiometric calibration of optical sensing instruments with traceability in solar reflective bands. *Opt. Precis. Eng.* **2015**, *23*, 1807–1812. [[CrossRef](#)]
34. Fox, N.; Aiken, J.; Barnett, J.J.; Briottet, X.; Carvell, R.; Frohlich, C.; Groom, S.B.; Hagolle, O.; Haigh, J.D.; Kieffer, H.H.; et al. Traceable Radiometry Underpinning Terrestrial and Helio-Studies (TRUTHS). *Proc. SPIE* **2003**, *4881*, 395–406.
35. Fox, N.; Weiss, A.K.; Schmutz, W.; Thome, K.; Young, D.; Wielicki, B.A.; Winkler, R.; Wooliams, E. Accurate radiometry from space: An essential tool for climate studies. *Phil. Trans. R. Soc. A* **2011**, *369*, 4028–4063. [[CrossRef](#)]
36. Fox, N. Developments in optical radiation measurement at NPL: Part 1. *Proc. SPIE* **2001**, *4450*, 140–154.
37. Roithmayr, C.M.; Lukashin, C.; Speth, P.W.; Gregg, K.; Kurt, T.; Wielicki, B.A.; Young, D. Clarreo Approach for Reference Intercalibration of Reflected Solar Sensors: On-Orbit Data Matching and Sampling. *IEEE Trans. Geosci. Remote Sens.* **2014**, *52*, 6762–6774. [[CrossRef](#)]
38. Sun, W.; Lukashin, C. Modeling polarized solar radiation from the ocean–atmosphere system for CLARREO inter-calibration applications. *Atmos. Chem. Phys.* **2013**, *13*, 10303–10324. [[CrossRef](#)]
39. Jin, Z.; Lukachin, C.; Gopalan, A.; Gopalan, A.; Sun, W. Correlation between SCIAMACHY, MODIS, and CERES reflectance measurements: Implications for CLARREO. *J. Geophys. Res. Atmos.* **2012**, *117*, D5. [[CrossRef](#)]
40. Gentile, T.R.; Houston, J.M.; Hardis, J.E.; Cromer, C.L.; Parr, A.C. National Institute of Standards and Technology high-accuracy cryogenic radiometer. *Appl. Opt.* **1996**, *35*, 1056–1068. [[CrossRef](#)] [[PubMed](#)]
41. Houston, J.M.; Rice, J.P. NIST reference cryogenic radiometer designed for versatile performance. *Metrologia* **2006**, *43*, 31–35. [[CrossRef](#)]
42. Benjamin, W.; Andre, F.; Wolfgang, F.; Suter, M.; Soder, R.; Schmutz, W. Spectrally integrated window transmittance measurements for a cryogenic solar absolute radiometer. *Metrologia* **2014**, *51*, 344–349.
43. Martin, J.E.; Fox, N.P. Cryogenic Solar Absolute Radiometer (CSAR). *Metrologia* **1993**, *30*, 305–308. [[CrossRef](#)]
44. Hoyt, C.C.; Foukal, P.V. Cryogenic radiometers and their application to metrology. *Metrologia* **1991**, *28*, 163–167. [[CrossRef](#)]
45. Pearson, D.A.; Zhang, A.M. Thermal-electrical modeling of absolute cryogenic radiometers. *Cryogenics* **1999**, *39*, 299–309. [[CrossRef](#)]
46. Fox, N.; Hayocks, P.; Martin, J.E.; Haq, I.U. A mechanically cooled portable cryogenic radiometer. *Metrologia* **1995**, *32*, 581–584. [[CrossRef](#)]
47. Wielicki, B.A.; Young, D.F.; Mlynczak, M.G.; Thome, K.J.; Leroy, S.; Corliss, J.; Anderson, J.G.; Ao, C.O.; Bantges, R.; Best, F.; et al. Achieving Climate Change Absolute Accuracy in Orbit. *Bull. Am. Meteorol. Soc.* **2013**, *94*, 1519–1539. [[CrossRef](#)]
48. Willson, R.C. Solar Total Irradiance Observations by Active Cavity Radiometers. *Sol. Phys.* **1981**, *74*, 217–229. [[CrossRef](#)]
49. Suter, M. Advances in Solar Radiometry. Ph.D. Thesis, University of Zurich, Zurich, Switzerland, 2014.
50. Kopp, G.; Heuerman, K.; Harber, D.; Drake, G. The TSI Radiometer Facility: Absolute calibrations for total solar irradiance instruments. *Proc. SPIE Int. Soc. Opt. Eng.* **2007**, *6677*, 667709.
51. Nicola, S.; Willson, R.C.; Lee, J.N.; Wu, D.L. Modeling Quiet Solar Luminosity Variability from TSI Satellite Measurements and Proxy Models during 1980–2018. *Remote Sens.* **2019**, *11*, 2569.
52. Ye, X.; Yi, X.L.; Fang, W.; Wang, K.; Luo, Y.; Xia, Z.W.; Wang, Y.P. Design and Investigation of Absolute Radiance Calibration Primary Radiometer. *IET Sci. Meas. Technol.* **2018**, *12*, 994–1000.
53. Fang, Q.Q.; Fang, W.; Wang, Y.P.; Ye, X.; Yu, B.X. New shape of blackbody cavity: Conical generatrix with an inclined bottom. *Opt. Eng.* **2012**, *51*, 086401. [[CrossRef](#)]

54. Yi, X.L.; Yang, Z.L.; Ye, X.; Wang, K.; Fang, W.; Wang, Y.P. Absorptance measurement for sloping bottom cavity of cryogenic radiometer. *Opt. Precis. Eng.* **2015**, *23*, 1–7.
55. Yi, X.L.; Fang, W.; Luo, Y.; Xia, Z.W.; Wang, Y.P. Correction of cavity absorptance measure method for cryogenic radiometer. *IET Sci. Meas. Technol.* **2016**, *10*, 564–569. [[CrossRef](#)]
56. Huang, L.K.; Cebula, R.P.; Hilsenrath, E. New procedure for interpolating NIST FEL lamp irradiance. *Metrologia* **1998**, *35*, 381–386. [[CrossRef](#)]



© 2020 by the authors. Licensee MDPI, Basel, Switzerland. This article is an open access article distributed under the terms and conditions of the Creative Commons Attribution (CC BY) license (<http://creativecommons.org/licenses/by/4.0/>).